Supporting Information

Material-electrolyte interfacial interaction enabling formation of inorganic-rich solid electrolyte interphase for fast-charging Si-based lithium-ion batteries

Kai Cheng[†,a,b]; Shuibin Tu[†,a]; Bao Zhang[a]; Wenyu Wang[a]; Xiaohong Wang[a]; Yucheng Tan[a]; Xiaoxue Chen[a]; Chunhao Li[a]; Chenhui Li[b]; *Li Wang[c];* and Yongming Sun[*,a]

a. *Wuhan National Laboratory for Optoelectronics, Huazhong University of Science and Technology, Wuhan 430074, China*

b. *State Key Laboratory of Material Processing and Die & Mould Technology, School of Materials Science and Engineering Huazhong University of Science and Technology, Wuhan 430074, Hubei, China*

c. *Institute of Nuclear & New Energy Technology, Tsinghua University, Beijing 100084, China.*

† *These authors contributed equally to this work.*

Electronic Supplementary Information (ESI) available: [details of any supplementary information available should be included h. See DOI: 10.1039/x0xx00000x

Corresponding author: yongmingsun@hust.edu.cn

1. Experimental Section

Synthesis: Commercial SiO_x powder was mechanically ball milled for 20 h at 350 rpm after being received. Red P was washed with deionized water and dried in a vacuum oven at 60 °C for 2 h to remove the natural oxide layer on its surface. SiO_x@P was synthesized via ball milling using the as-obtained SiO_x powder and red P powder in the weight ratio of 97: 3 an Ar atmosphere for 6 h at 350 rpm.

Electrolyte preparation: 1.3 M $LiPF_6$ in ethylene carbonate (EC) / ethyl methyl carbonate (EMC) (EC / EMC = 3 / 7 by volume fraction) (LP), fluoroethylene carbonate (FEC), and vinylene carbonate (VC) were purchased from Duoduo Chemical Technology Co., LTD (Suzhou, China). The electrolyte consists of LP with 1 wt.% VC and various content of FEC additives (0, 5, 10, 20, 30 wt.%, denoted as LP0, LP5, LP10, LP20, and LP30, respectively) were prepared in an Ar-filled glove box (water and oxygen contents < 0.01 ppm) according to the weight value presented in Table S1. The LP20 was used in this work for testing, otherwise stated.

Structural Characterizations: X-ray diffraction (XRD) was conducted using a Philips X' Pert diffractometer with Cu Kα radiation (λ = 1.5418 Å) to identify the phase information of the samples. Scanning electron microscopy (SEM) and energy dispersive X-ray spectroscopy (EDS) mapping of samples were performed by a GeminiSEM300 field-emission SEM under an acceleration voltage of 5 kV. X-ray photoelectron spectra (XPS) measurements were carried out on an AXIS-ULTRA DLD spectrometer with Al Kα radiation. Transmission electron microscope (TEM), high-resolution TEM (HRTEM), high-angle annular dark-field scanning TEM (HAADF-STEM), energy dispersive X-ray (EDX) mapping images (STEM-EDS), and selected area electron diffraction (SAED) patterns were acquired using FEI Talos f200x, working on an acceleration voltage of 200 kV. Derjaguin-Muller-Toporov (DMT) modulus images were obtained from commercial atomic force microscopy (AFM, Bruker Multimode 8 with a Nanoscope V controller) using an insulating silicon AFM tip (k = 26 N m⁻¹, f_0 = 300 kHz) in an argon-filled glove box with peak force tapping mode. The force-displacement curves were analyzed by Nanoscope Analysis software. Raman spectroscopy was performed on a Renishaw RM2000 confocal Raman spectrometer with a 532 nm excitation laser (laser spot size of 0.5 μm) operated at a low power level (~ 2 mW). Fourier transform infrared (FT-IR) spectra were obtained by Bruker Vertex 70 equipped with an Attenuated Total Reflectance (ATR) module with a scanning range of 400-4000 cm⁻¹ at room temperature. For ex-situ characterizations of SEM, TEM, Raman, and FTIR, the cells were disassembled in an Ar-filled glove box, and the electrodes were collected and washed with dimethyl carbonate (DMC) to remove any residual Li salts from the surface of the electrodes.

Electrochemical Characterizations: The SiO_x@P and SiO_x electrodes consisted of active materials, super P, and PAA binder with a weight ratio of 8:1:1, which were fabricated through a slurry method. CR2032 coin-type half cells were assembled in an Ar-filled glove box using Celgard 2500 polypropylene (PP) membrane as the separator. In a typical half cell, a 3-cycle 0.1 *C* formation process was conducted before the test (1 *C* = 1500 mAh g⁻¹), and the voltage range for cycling was 0.01−1.0 V (*vs.* Li⁺/Li). The $LiNi_{0.6}Co_{0.2}Mn_{0.2}O_2$ (NCM622) electrodes consisting of active materials (90 wt.%), super P (5 wt.%), and polyvinylidene fluoride (PVDF, 5 wt.%) were used for full pouch cell assembly. The typical mass loadings of the anode and cathode were ~ 1.8 and 9.3 mg cm⁻², respectively. The details of the Ah-level NCM622||SiO_x@P laminated pouch cell were listed in Table S4. The galvanostatic charge/discharge measurement voltage range was 2.5–4.2 V for NCM622||SiO_x-based full cells. The charging protocol for full cells was optimized with the combination of constant current and constant voltage

(CCCV) charging. The current densities for CC charging varied from 1 to 6 C (1 C = 1.67 mA cm^{-2}). The CV charging was conducted at 4.2 V for the NCM622 cathode. The corresponding total charging times (CC+CV) were fixed at 60 min, 30 min, 20 min, 15 min, and 10 min for 1C-CV, 2C-CV, 3C-CV, 4C-CV, and 6C-CV, respectively. The discharging current was set at 0.2 C. The full pouch cells were tested in the voltage range of 2.5–4.2 V. Before the assembly of the full pouch cell, the SiO$_x$@P and bare SiO$_x$ electrodes were electrochemically pre-cycled in Li metal half cell (1 cycle). Energy density was calculated based on the total weight of the cathode and anode (excluding the mass of the current collector). Galvanostatic charge/discharge measurements were performed on the Neware battery testing system (CT-4008T-5V-50mA-164, Shenzhen, China). Galvanostatic intermittent titration technique (GITT) measurements were performed on LAND CT2001A testing instruments. The electrochemical impedance spectroscopy (EIS), cyclic voltammetry (CV), linear sweep voltammetry (LSV), and alternating current (AC) voltammetry were conducted on a Biologic VMP3 electrochemistry workstation. The EIS was tested in the 100 mHz-100 KHz frequency range with an amplitude of 10 mV. The alternating current (AC) voltammetry test was conducted in the 1.0 to 3.0 V (*vs.* Li$^+$/Li) potential range with a frequency of 10 Hz and an amplitude (A) of 5 mV.

Calculation methods: The DFT calculations were conducted utilizing the Vienna Ab-initio Simulation Package (VASP),[1], which was based on the Projector Augmented Wave (PAW) method.[2] The exchange-correlation function employed was the Perdew, Burke, and rnzerhof (PBE) form, along with van der Waals corrections using the DFT-D3 method.[3] The kinetic energy cutoff for the electronic wave function was set to 520 eV. Brillouin zone sampling was carried out using the Monkhorst−Pack scheme.[4] The adsorption energies (E$_{ads}$) were calculated as follows:

$$E_{ads} = E_{slab\text{-}ads} - E_{slab} - E_{ads}$$

Where E$_{slab\text{-}ads}$ is the total energy of species adsorbed surface, E$_{slab}$ is the energy of SEI surface, and E$_{ads}$ is the energy of adsorbed species, respectively.

Classical molecular dynamics simulations (MD) were conducted using LAMMPS.[1] The initial periodic systems were constructed through PACKMOL and Moltemplate (http://www.moltemplate.org/).[2] For the solvents, we employed the OPLS force-field parameters combined with RESP charges.[5] The CVFF force-field parameters were also utilized for P, SiO, and Si.[6,7] The parameters for Li$^+$ and PF$_6^-$ ions were obtained from previous reports.[8,9] Throughout the simulations, the electrodes were held fixed. Initially, Langevin dynamics were applied to randomize the initial molecular configurations at 500 K for 1 ns. Subsequently, the simulation proceeded with NVT runs at 500 K for 1 ns to achieve system equilibrium.[8] Following this, a 10 ns NVT run was conducted at 300 K. The electric double layer (EDL) structures were determined by statistically analyzing the data from the final 5 ns of the trajectory. VESTA and VMD were employed for visualizing the electrolyte structures.[10]

Note S1: The SiO$_x$@P (3%) material was synthesized by a simple chemomechanical reaction between the pristine SiO$_x$ and red P, as illustrated in Fig S1a. The STEM-EDS mapping image recorded on the SiO$_x$@P particle in Fig. S1b showed a relatively uniform distribution of P elements outside the SiO$_x$ surface, reflecting a ~ 6 nm-thick P layer (Fig. S1c). Compared to the XRD patterns of the SiO$_x$@P and SiO$_x$ powder in Fig. S1d, the SiO$_x$@P exhibited the typical diffusion regions without prominent peaks, indicating no formation of a new crystalline phase. Moreover, the P *2p* high-resolution XPS spectra of the SiO$_x$@P and bare P revealed that two peaks located at ~ 135.2 eV and ~ 134.5 eV were related to the formation of covalent P-O-Si and P-O bonds between the SiO$_x$ and P,[11] which confirmed a firm bonding of P interphase on SiO$_x$ surface (Fig. S1e). For the Si *2p* XPS spectra of the SiO$_x$@P and SiO$_x$ (Fig. S1f), four of all the peaks belonged to Si^{4+}, Si^{3+}, Si^{2+}, and Si^{1+} of amorphous SiO$_x$ slightly shifted right, and with the addition of phosphorus, the signal intensity of silicon in its oxidized state also obviously increased, closely associated with the stronger electronegativity of O than P.[12] SEM images of the pristine SiO$_x$ before and after ball-milling in Fig. S2 (a-d) revealed that both the SiO$_x$@P and SiO$_x$ after ball-milling were composed of nanosized particles with diameters ranging from 100 to 800 nm.

Note S2:

To better understand the different specific adsorption behavior of the FEC molecule, SiO$_x$@P ‖ Li and SiO$_x$ ‖ Li cells were assembled using the LP5, LP10, LP20, and LP30 electrolytes, respectively, and subjected to the following CV and the galvanostatic charge/discharge measurements. The CV curves in Fig. S14a, b exhibited the more pronounced reduction peak at ~ 1.25 V (*vs*. Li$^+$/Li) corresponding to FEC reduction in the anodic scanning process for all the SiO$_x$@P based cells compared to the bare SiO$_x$-based cell,[13] suggesting that the interfacial interaction was dependant on the active material interface design rather than the solvation sheath structure of Li$^+$ or the FEC concentration in bulk electrolytes. Combined with the apparent potential plateau ~ 1.22 V (*vs*. Li$^+$/Li) of the SiO$_x$@P than that of the bare SiO$_x$ in the first cycle charge-discharge profiles (Fig. S14c, d),[14] further verifying the as-forementioned preferential adsorption and catalytic reduction behavior of FEC molecule in the inner Helmholtz plane (IHP). As shown in Fig. S16a, b, the SiO$_x$@P cycled in the LP10, LP20, and LP30 electrolytes all exhibited high reversible capacities (> 1050 mAh g^{-1}) at 1.0 C and excellent capacity retention rate (> 80%) at 500 cycles. In contrast, the bare SiO$_x$ lost almost all its capacity and delivered a low capacity of less than 400 mAh g^{-1} under the same test condition. Notably, the LP20 electrolyte showed the best cycling performance among those electrolytes through optimization. Therefore, the LP-20 was used in this work for testing, otherwise stated.

Note S3:

SiO$_x$-P composites with different P contents (1, 3, and 9 wt.%) were fabricated, and their electrochemical performance evaluations were conducted (Fig. S18). SiO$_x$-P composites containing 1 wt.% P demonstrated inferior cycling stability in comparison to SiO$_x$@P composites with 3 wt.% P, a phenomenon potentially attributable to the incomplete P/Li$_3$P protection layer. SiO$_x$@P composites with 9 wt.% P manifested a lower specific capacity and inferior cycling stability. These characteristics are likely due to the increased cell polarization (Fig. S18a) and resistance (Fig. S18c), resulting from the too-thick layer of the P layer.

Note S4:

The fitted values of the R_{SEI} for Fig. 3f, g, according to the Arrhenius equation:[15]

$$\frac{T}{R_{SEI}} = A \, e^{-\frac{E_a}{RT}}$$

Wher T, R_{SEI}, A, E_a and R represent the absolute temperature in kelvin, the resistance of Li$^+$ through the SEI, pre-exponential factor, activation energy, and standard gas constant, respectively. The activation energy E_a is obtained by fitting the semicircles (R_{SEI}) in the high-middle frequency range of the symmetric cells. R_{SEI} represents the resistance of Li$^+$ transport through the SEI film.

2. Supplementary Figures
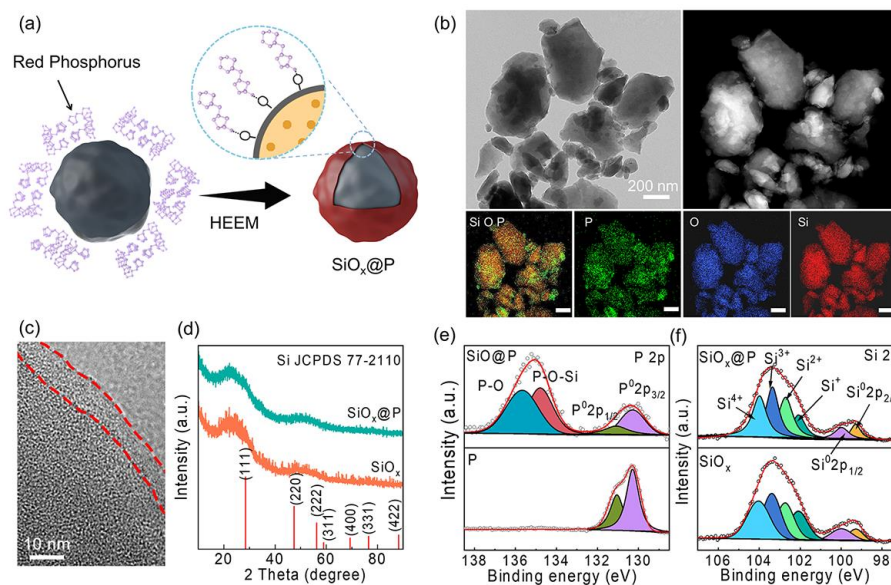
Fig. S1 (a) Schematic for the synthesis of the SiO$_x$@P composite. (b) TEM image, STEM-HADDF images, and the corresponding Si, O, and P elements EDS mapping images, (c) high-resolution TEM image for the SiO$_x$@P particles. (d) XRD patterns of the SiO$_x$@P and bare SiO$_x$. (e) High-resolution P *2p* XPS spectra for the SiO$_x$@P and red P. (f) High-resolution Si *2p* XPS spectra of the SiO$_x$@P and bare SiO$_x$.
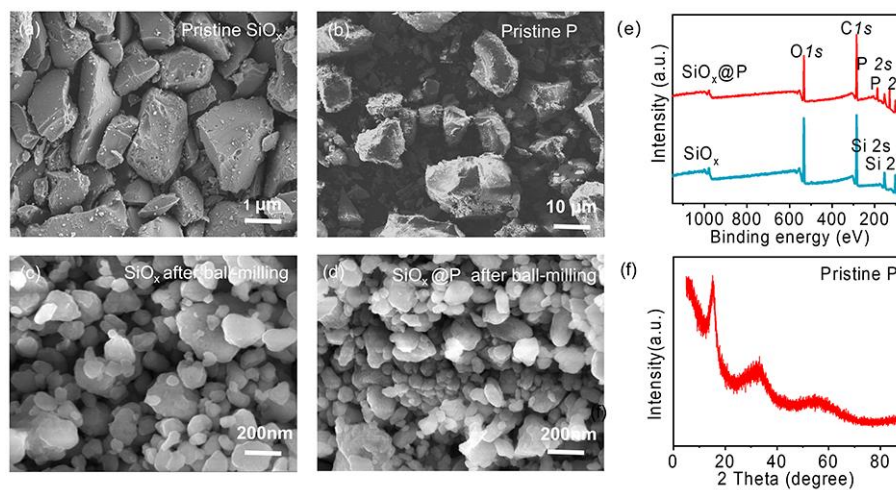
Fig. S2 SEM images of (a) pristine SiO$_x$, (b) pristine red P, (c) bare SiO$_x$, and (d) SiO$_x$@P after ball milling. (e) Full survey XPS spectra of the bare SiO$_x$ and SiO$_x$@P composite. (f) XRD pattern of the pristine P.
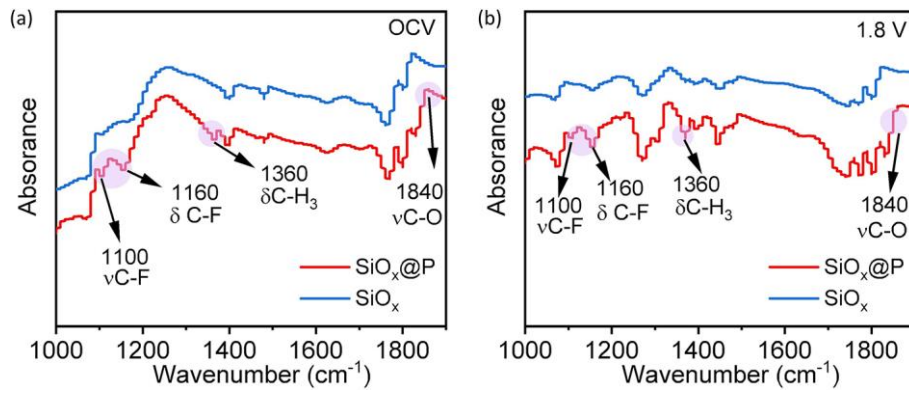
Fig. S3 (a) The *ex*-situ Fourier transform infrared spectroscopy (FTIR) spectra of the SiO$_x$@P, and bare SiO$_x$ electrodes at an open current voltage (OCP) and discharging to 1.8 V.
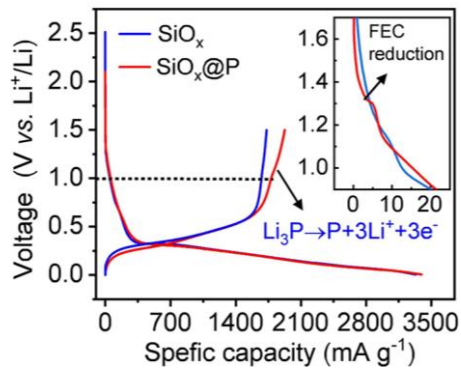
Fig. S4 Charge/discharge profiles for the SiO$_x$@P||Li and SiO$_x$||Li cells after charging to 1.5 V.

Schematic description of IHP with improving specific adsorption of FEC after P coating
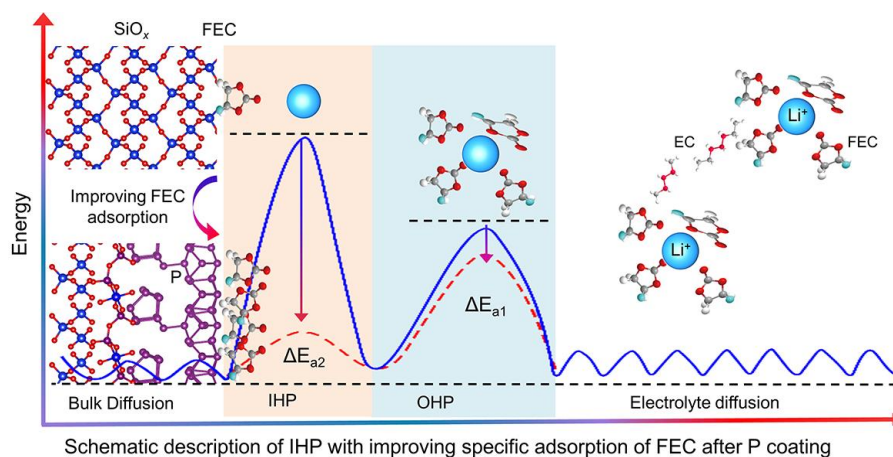
Fig. S5 Schematic description of IHP with specific adsorption of FEC.

As illustrated, the interfacial chemistry of the SEI was correlated with the initial SiO_x surface adsorption electrical double layer at the nanoscale. Under the premise of the constant solvation sheath structure of Li^+ in bulk electrolytes, the adsorption behavior of FEC molecules in IHP could be altered by introducing a functional P interphase layer on the SiO_x surface. The activation energies (Ea) of the journey of Li^+, including the desolvation energy of Li^+ (Ea_1) and Li^+ transportation in SEI film (Ea_2), could be significantly influenced after P coating.
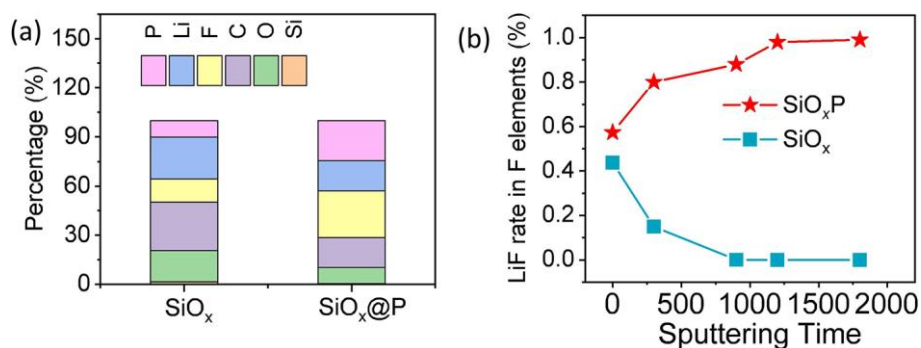
Fig. S6 (a)The atomic ratios of diverse elements. (b) The F atomic mass proportion of LiF in fluorides (including $Li_xP_yFO_z$ /Li_xPF_y, C-F bond, and LiF species) in the bare SiO_x and $SiO_x@P$ electrodes according to the XPS fitting results in Fig 2 (a, b).
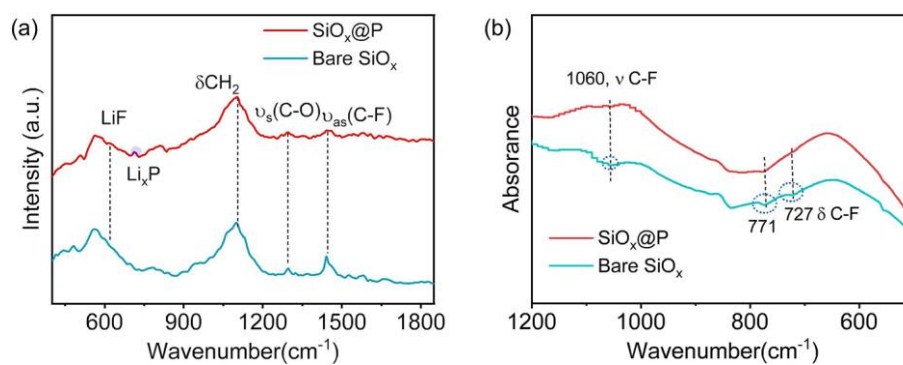
Fig. S7 The *ex*-situ Raman (a) and FTIR spectra (b) of the bare SiO_x and $SiO_x@P$ electrodes after the formation cycle.

As shown in Fig. S6a, two peaks at ~ 610 cm^{-1} and ~ 720 cm^{-1}, attributed as LiF and Li_xP species, respectively, were evident in the interphase on the $SiO_x@P$.[16] The result supported the formation of Li_3P/LiF-rich SEI on $SiO_x@P$. The FTIR spectra of SiO_x after the formation cycle exhibited three distinct peaks at 727,771, and 1060 cm^{-1}, respectively, features absent in the bare $SiO_x@P$ electrode.
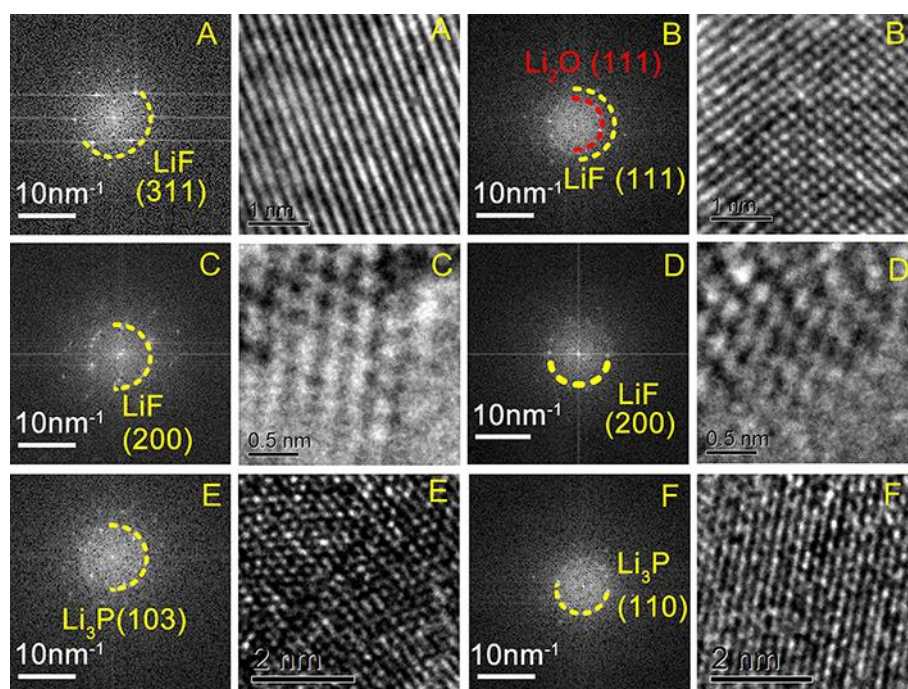
Fig. S8 Selected area electron diffraction (SAED) patterns and the corresponding FFT patterns of the A-F regions of the SiOx@P interphase (Fig. 2 c).
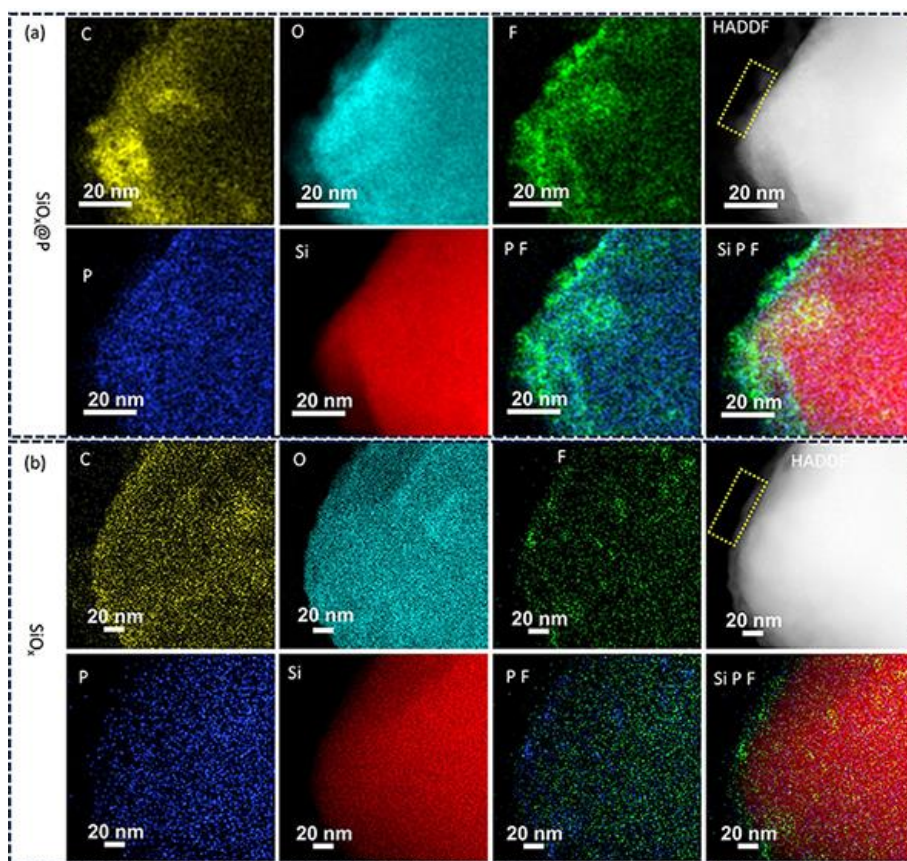
Fig. S9 The STEM-EDS mapping of (a) the SiO$_x$@P and (b) bare SiO$_x$ electrodes after the formation cycle.
The atomic ratio analysis was conducted on the regions marked by the yellow dot line rectangle. The results were shown in Fig.S10 and Table S3, demonstrating the higher F and P content on the surface of the SiO$_x$@P compared to the bare SiO$_x$ electrodes.
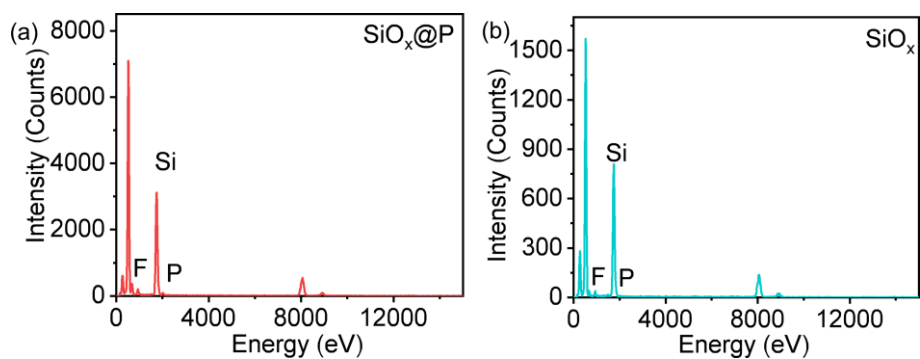
Fig. S10 The STEM-EDS spectra results for the marked regions of (a) the SiO$_x$@P and (b) the bare SiO$_x$ electrodes after the formation cycle.
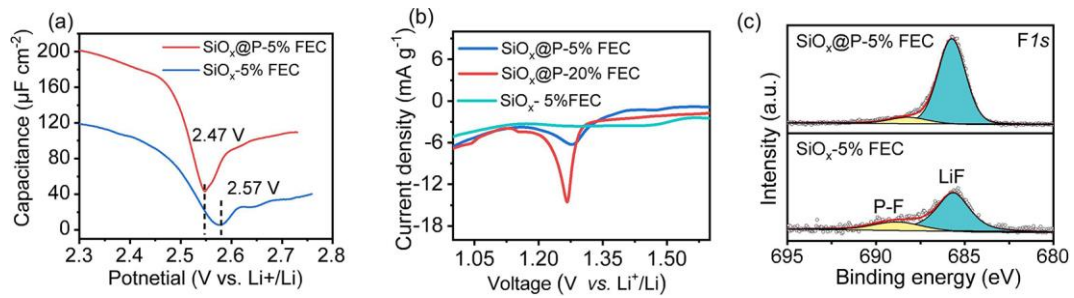
Fig. S11 (a)The non-Faradaic capacitance-potential curves for the different SiO_x half cells at 2.3–2.8 V using LP5 electrolyte. (b) Initial CV curves of the different SiO_x half cells at a scanning rate of 0.01 mV s^{-1} between 1.0–1.7 V using LP5 and LP20 electrolytes, respectively. (c) The high-resolution F1s XPS spectra of the SiO_x@P and SiO_x electrodes after the formation cycle using LP5 electrolyte.

    The SiO_x@P demonstrated a distinct change in the potential of zero charge (PZC) in the capacitance-potential curves (2.47 vs. 2.57 V for PZC), and a more noticeable FEC reduction peak at ~ 1.25 V in the CV curves compared to that of the bare SiO_x using LP5 electrolyte (Fig. S11a, b). In addition, the LiF component in the SEI on the SiO_x@P electrode, mainly derived from the decomposition of FEC, was higher than that of the bare SiO, as evidenced by the higher peak intensity in the high-resolution F1s XPS spectra, further confirming the enhanced FEC-specific adsorption and catalytic decomposition (Fig. S11c).
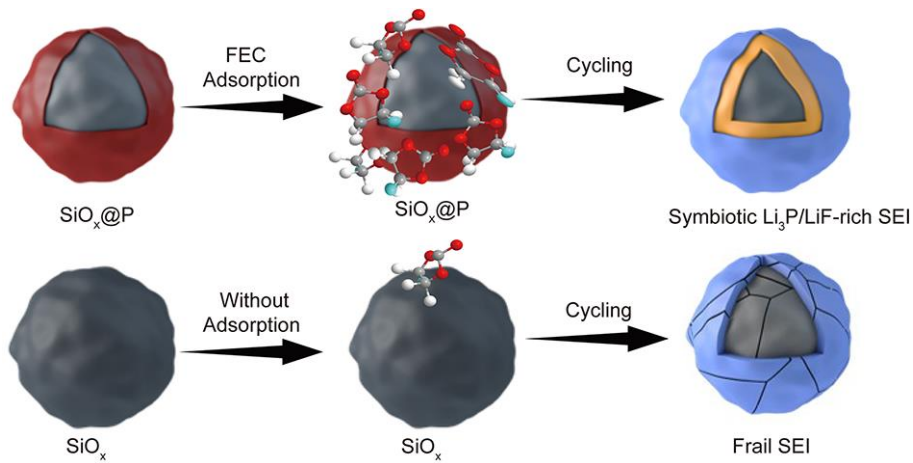
Fig. S12 Schematic illustration of SEI evolution on the SiO_x@P and bare SiO_x anodes.
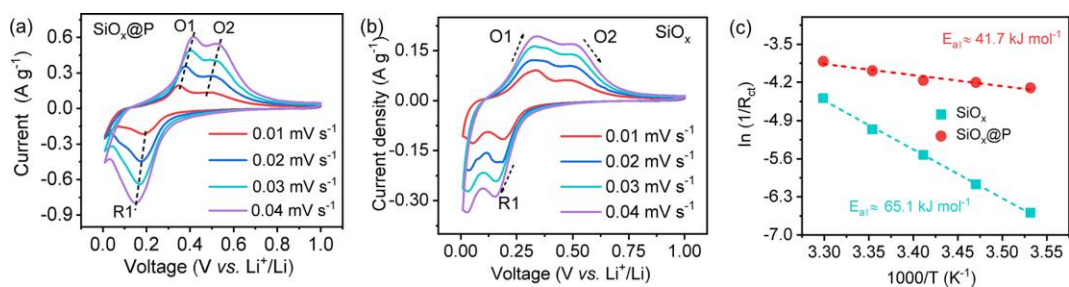
Fig. S13 CV curves of the SiO$_x$@P (a) and bare SiO$_x$ (b) electrode at different scan rates. Arrhenius behavior and activation energies (E_{a1}) of Li$^+$ desolvation (c).
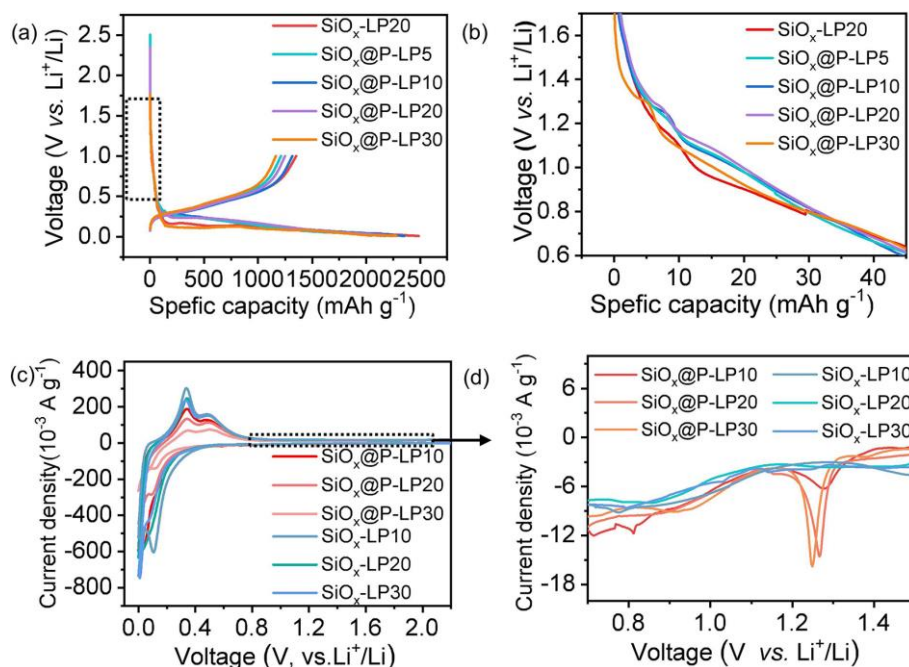
Fig. S14 (a) The first-cycle charge and discharge profiles of the SiO$_x$@P and bare SiO$_x$ anode using the LP5, LP10, LP20, and LP30 electrolytes at 0.1 *C*. (b) The enlarged images of the charge and discharge profiles in a. (c) CV curves and the enlarged ones (d) of the bare SiO$_x$ and SiO$_x$@P electrodes using the LP10, LP20 and LP30 electrolytes with scan rate of 0.01mV s^{-1}.
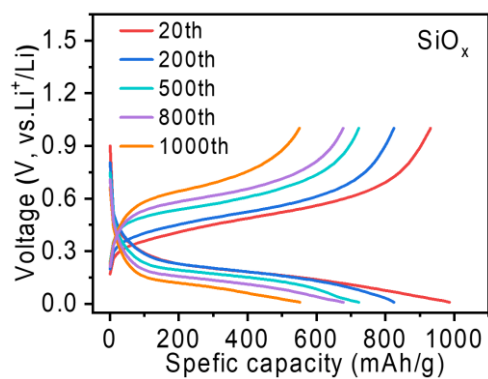
Fig. S15 The Charging/discharging profiles of the bare SiO$_x$ at different cycles.
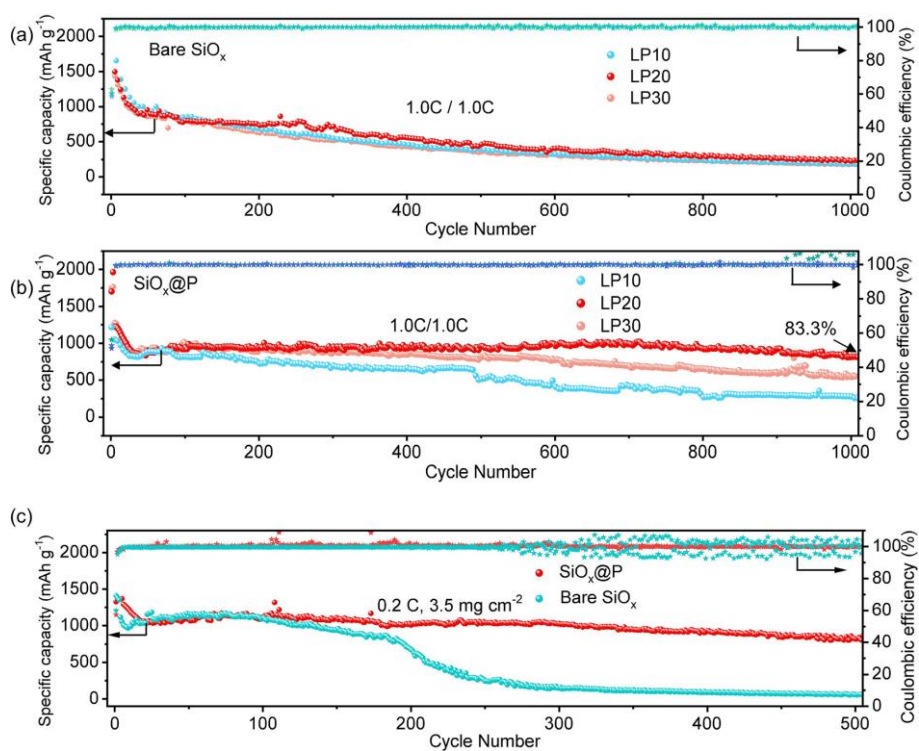
Fig. S16 CE and cycling performance of the SiO$_x$||Li (a) and SiO$_x$@P||Li (b) cells using the LP10, LP20, and LP30 electrolytes. (c) The CE and cycling performance of SiO$_x$@P||Li and SiO$_x$||Li cells where the anode with high active materials loading of 3.5 mg cm^{-2} using the LP20 electrolyte.

11
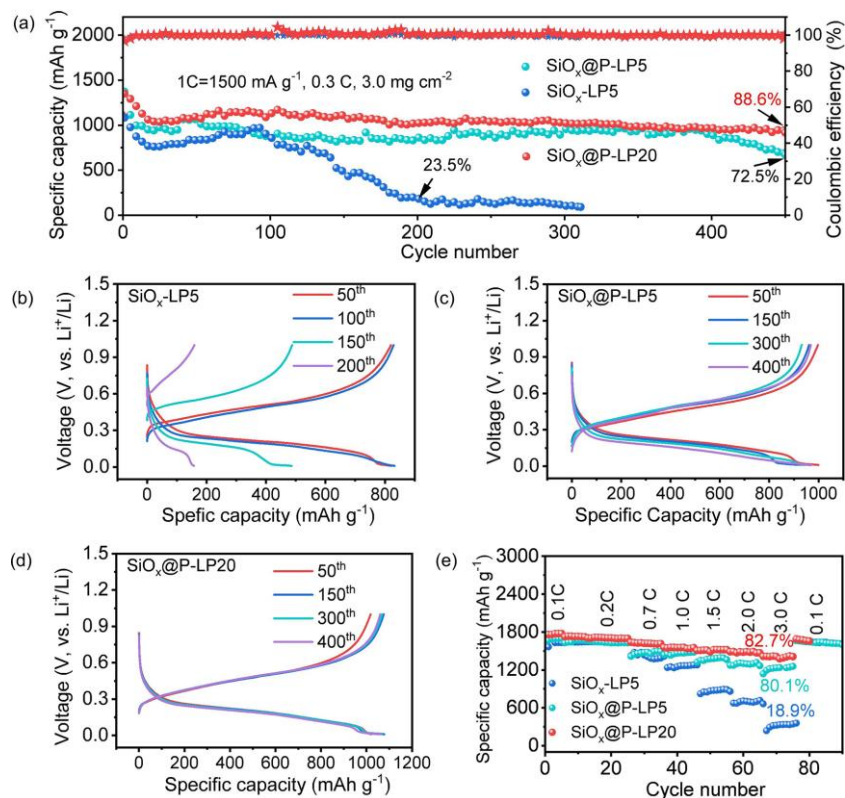
Fig. S17 Electrochemical performance of different SiO_x electrodes with half-cell configuration (active materials loading of ~3.0 mg cm^{-2}) using LP5 and LP20 electrolytes, respectively. (a) Cycling performance, (b-d) the corresponding selected charging/discharging profiles cycled at 0.3 C and (e) rate capability of the electrodes.

Upon the utilization of LP5, SiO_x@P exhibited an impressively extended cycling lifespan (72.5% capacity retention at the 450th cycle, in contrast to 23.5% at the 200th cycle) and an improved rate capacity relative to the uncoated SiO_x (80.1% versus 18.9% in terms of capacity retention).
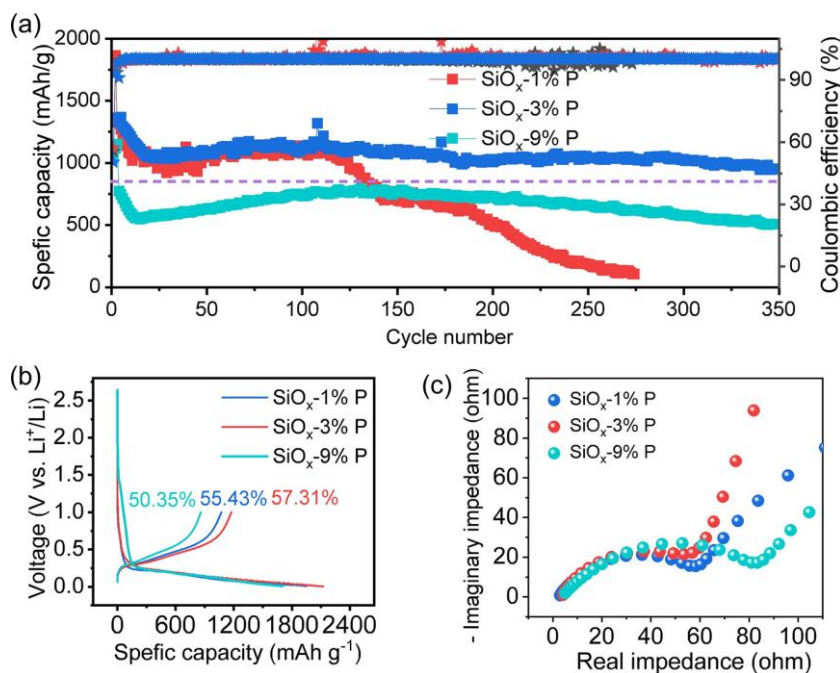
Figure S18. Capacity-cycle number (a) and voltage-capacity plots (b) of SiO_x-P composite with different P contents. (c) Nyquist plots of the SiO_x-P (1%, 3%, 9%) nanocomposite electrodes after 10 cycles.

12
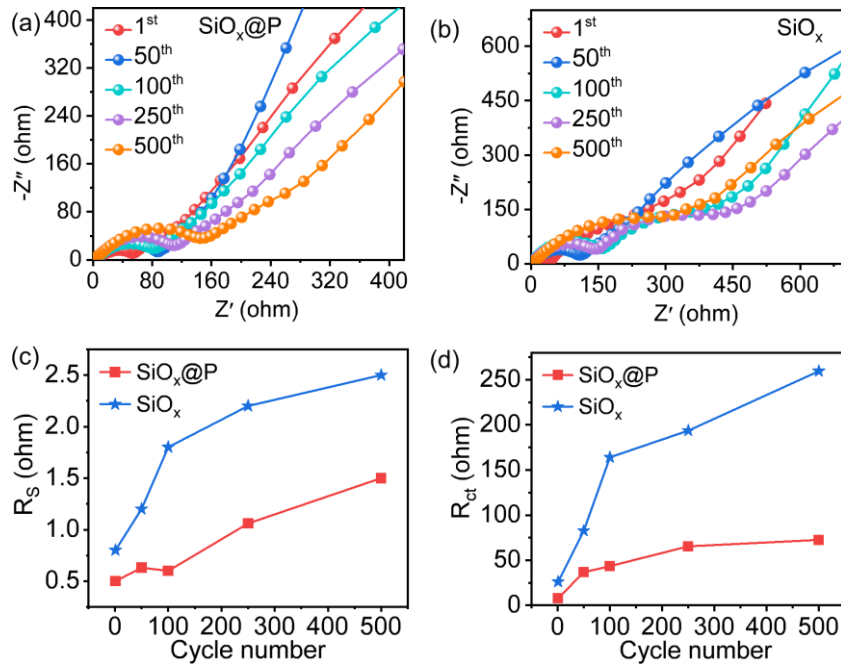
Fig. S19 (a, b) EIS profiles of the SiO_x@P and the bare SiO_x after different cycles at 1.0 C. Fitted values of the R_s (c) and R_{SEI} (d) for SiO_x@P||Li and SiO_x||Li coin cells after 1, 50, 100, 250, 500 cycles under at 1.0 C.
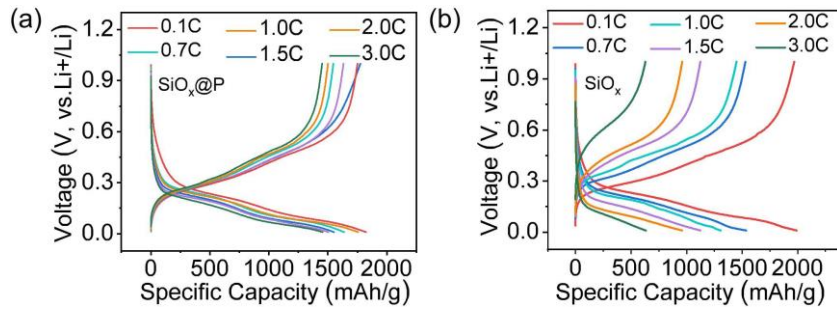
Fig. S20 Charging/discharging profiles of the bare SiO_x (a) and SiO_x@P (b) at different current densities.
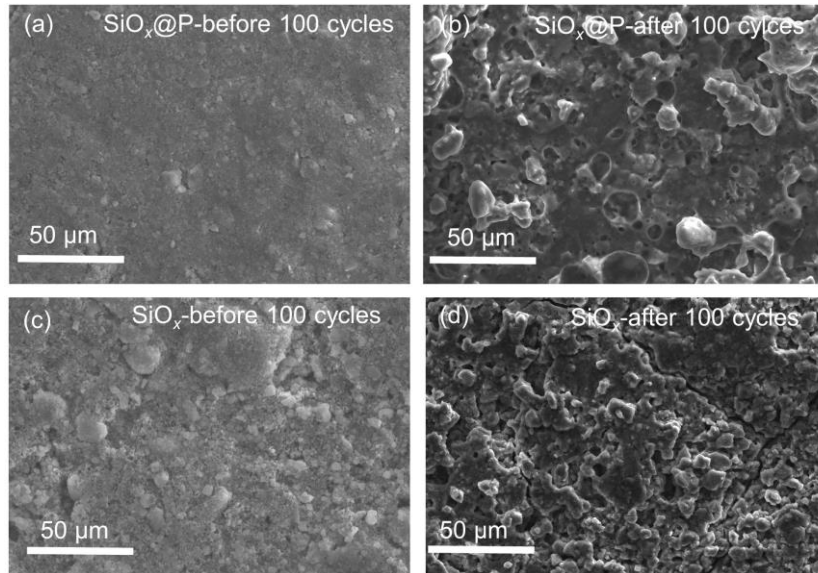
Fig. S21. SEM images of the SiO$_x$@P (a, b) and bare SiO$_x$ (c, d) before and after 100 charge/discharge cycles at 1.0 C.
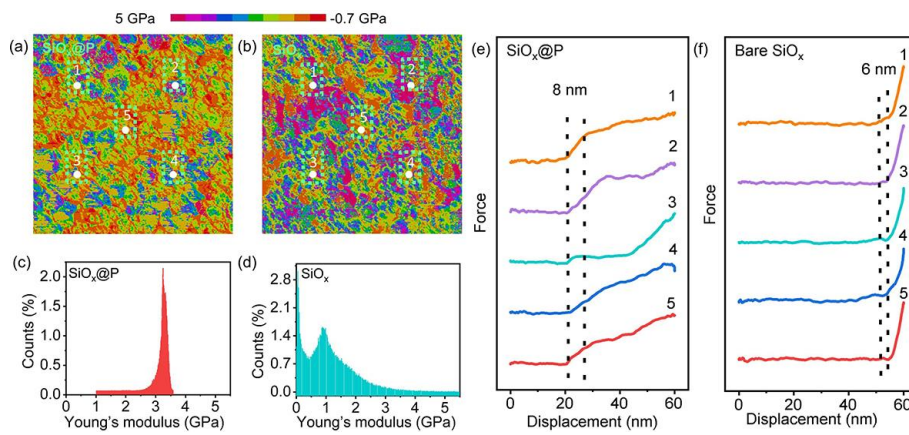
Fig. S22. 2D Derjaguin–Muller–Toporov (DMT) modulus mappings, Young's modulus distribution curves, force-displacement curves from the white points in the corresponding 2D DMT modulus mappings of the SEI on the SiO$_x$@P (a, c, e) and SiO$_x$ (b, d, f) anode after 100 cycles.

14
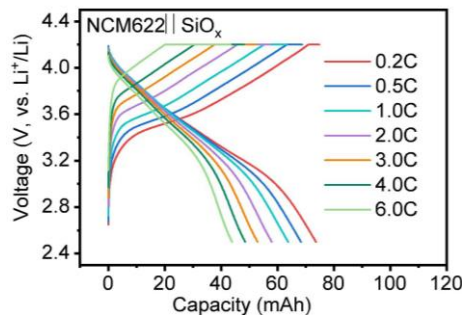
Figure S23. Charge/discharge profiles of NCM622||SiOx single-layer pouch cell at various current densities.
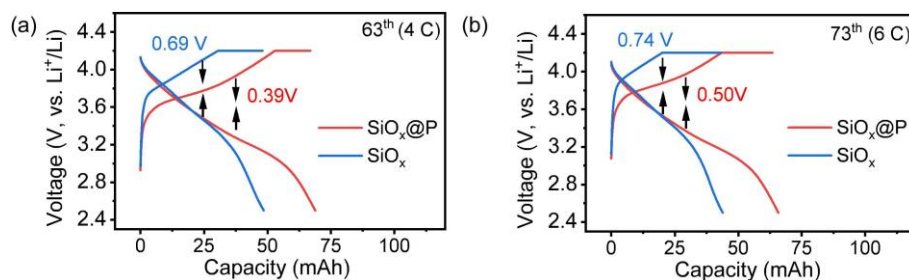
Figure S24. Comparison of the difference value median voltage difference values for the cells. Charge/discharge voltage profiles of NCM622||SiOx@P and NCM622||SiOx single-layer pouch cycled at 4 *C* (a) and 6 *C* (b) charging rates, respectively.
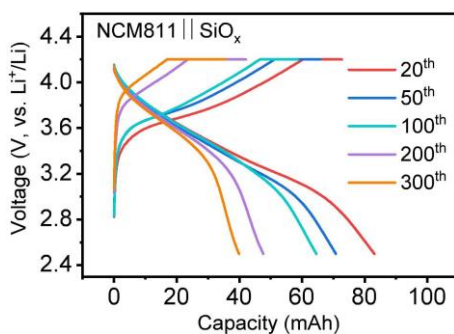
Figure S25. Charge/discharge profiles NCM622||SiOx single-layer pouch cell at 4 *C* (corresponding to a charging time of 15 minutes) for different cycles.

15
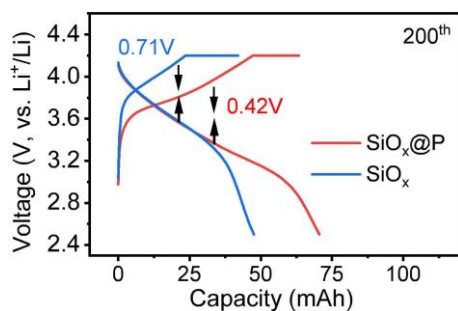
Figure S26. Comparison of the difference value median voltage difference values for the cells. Charge/discharge voltage profiles of NCM622||SiO$_x$@P and NCM622||SiO$_x$ single-layer pouch after 200 cycles at 4 C charging rate.
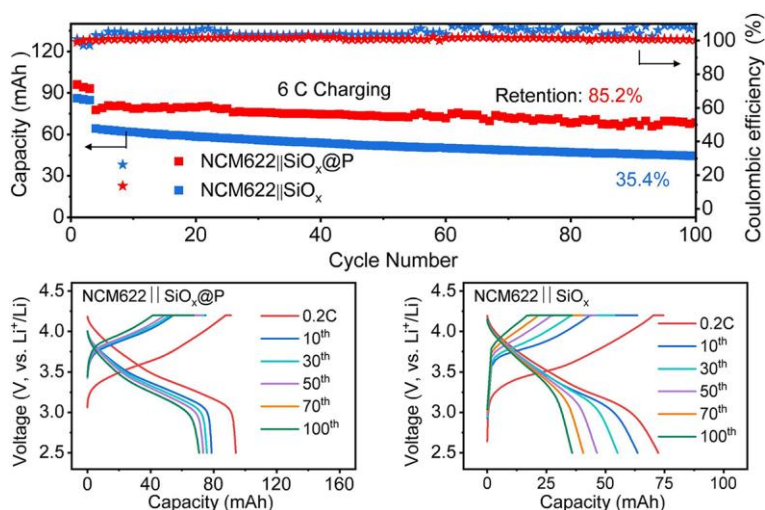
Figure S27. Cycling performance (a) and the charging/discharging profiles (b, c) of the pouch cells with different SiO$_x$ anodes at a charging rate of 6 C.

The pouch cell based on SiO$_x$@P anode achieved an unmatched 100-cycle lifespan with 85.2% capacity retention at 6 C. In contrast, the cell based on bare SiO$_x$ anode showed lower capacity retention (35.4%) after 100 cycles at 6 C, along with increased overpotential and polarization during cycling, indicating rapid capacity degradation.
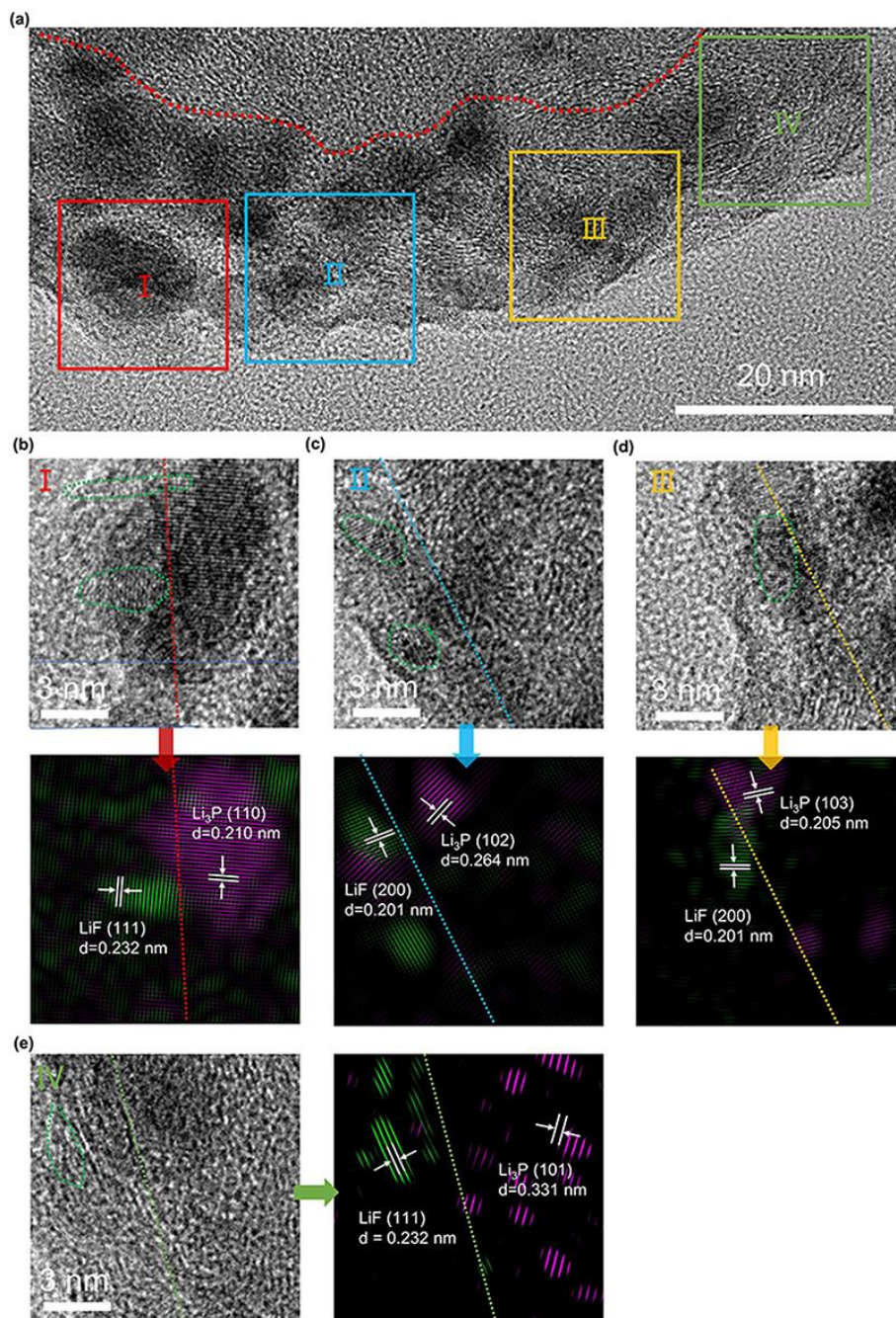
Figure S28. (a) HRTEM images of SiO$_x$@P after 100 cycles with a charging current density of 4 *C*. (b-f) Magnified images of Region Ⅰ (b), Region Ⅱ (c), Region Ⅲ (d), Region Ⅳ (e) and Region Ⅴ (f) outlined in (a) and the corresponding Fourier transform images.
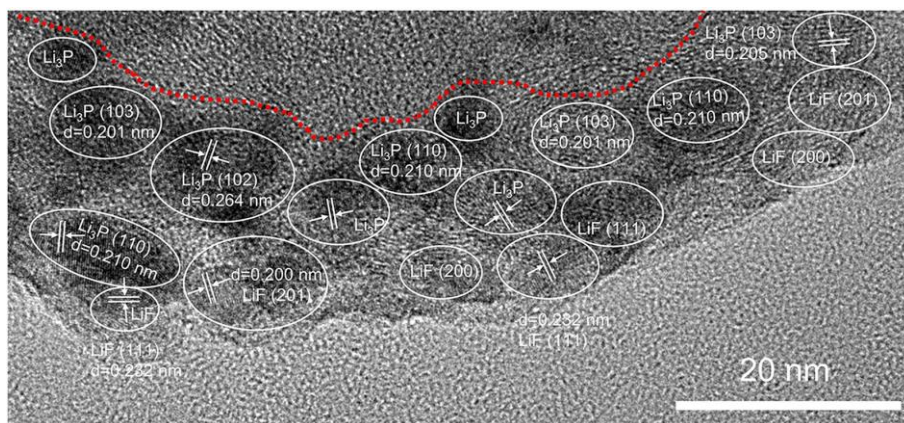
Figure S29. HRTEM images of SiO$_x$@P anode after 100 cycles with a charging current density of 4 *C*.

An SEI inner layer rich in Li$_3$P and outer layer rich in LiF, resembling a pseudo-bilayer, can be observed and confirmed as shown in Fig. S28, 29. It could be precisely described as symbiotic Li$_3$P/LiF-rich SEI.
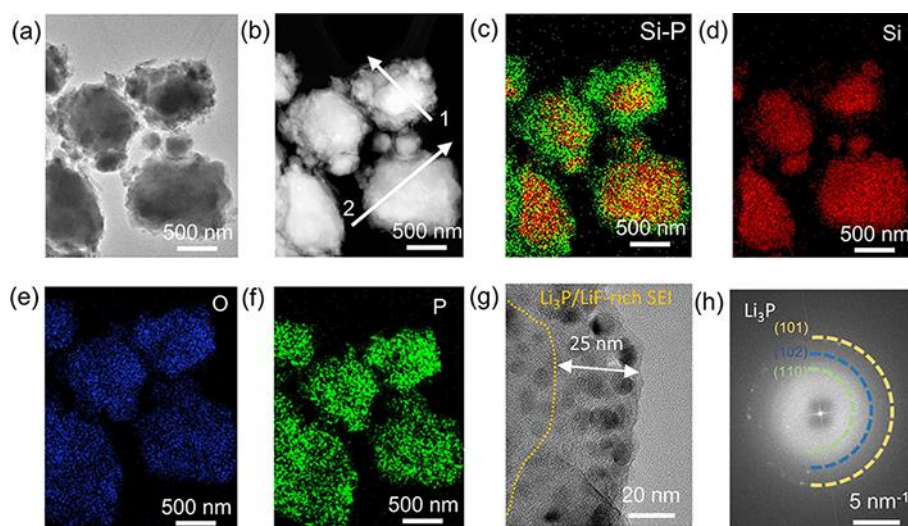
Figure S30. Bright-field (a), Dark-field TEM image (b), elemental mapping images (c–f), high-resolution TEM (g), and the corresponding SEAD images (h) of the SiO$_x$@P materials after 200 charge/discharge cycles at 4 *C*.
The diffraction spots in the diffraction pattern align with the (110) and (120) crystal planes of Li$_3$P.
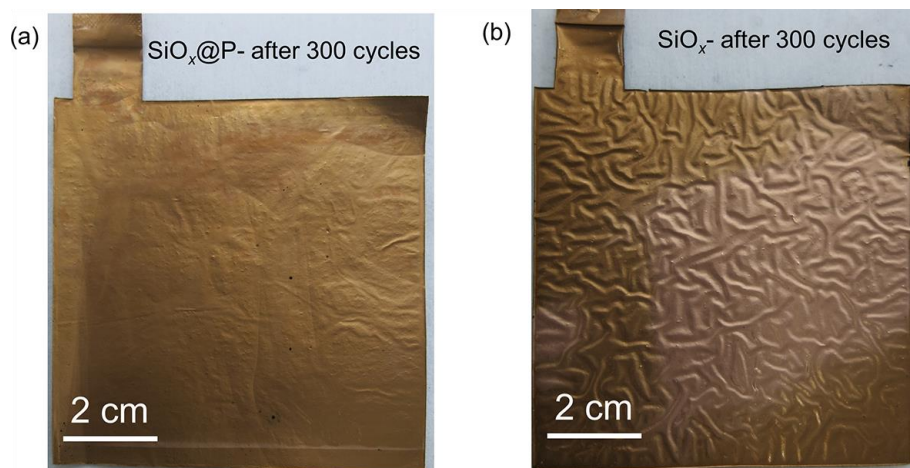
Figure S31. The optical images of Cu foils for (a) the SiO$_x$@P and (b) the bare SiO$_x$ anodes in the pouch cell after 300 cycles at 4 C.

3. Supplementary Tables

Table S1. The details of the electrolytes.

	1.3M LiPF$_6$ in EC/EMC (g)	FEC (g)	VC (g)
LP0	4.9	0	0.1
LP5	4.65	0.25	0.1
LP10	4.4	0.5	0.1
LP20	3.9	1.0	0.1
LP30	3.4	1.5	0.1

Table S2. XPS peak assignments for analyzing the compositions and chemical states of the interphases on anodes.

	C 1s (eV)	O 1s (eV)	VC (eV)
Hydrocarbon	284.8		
ROCO$_2$Li	287.2-290.0	532	
Li$_2$CO$_3$		532	
Li$_2$O	529.5		
Li$_x$P$_y$FO$_z$		533.3	686.1
Li$_x$PF$_y$			687.5
LiF			684.8

Table S3. The atomic fraction and mass fraction results of the EDS measurement were conducted on the interphases on the bare SiO$_x$ and SiO$_x$@P electrodes after the formation cycle.

	Bare SiO$_x$		SiO$_x$@P	
	Atomic fraction	Mass fraction (%)	Atomic fraction (%)	Mass fraction (%)
F	4.66	3.20	13.53	9.55
Si	94.66	96.04	84.56	88.25
P	0.68	0.76	1.91	2.20

Table S4. The detailed parameters of laminated NCM622|| SiO$_x$@P pouch cell.

	Parameter	Value
NCM622 Cathode	Specific capacity	176 mAh g^{-1} (cut-off voltage 4.2V)
	Area weight (each side)	1.64 mAh cm^{-2}
	Area capacity (each side)	9.3 mg cm^{-2}
	Number of layers	7
Al foil	thickness	12 μm
SiO$_x$@P anode	Specific capacity	1050 mAh g^{-1}
	Area weight (each side)	1.8 mg cm^{-2}
	Area capacity (each side)	1.89 mAh cm^{-2}
	Number of layers	8
Cu foil	Thickness	20 μm
Separator	Thickness	14 μm
	loading	0.726 mg cm^{-2}
Electrolyte	E/C ratio	3.8 g Ah^{-1}
Package foil	Thickness	153 μm
	Average Voltage	3.4V
Pouch cell	Capacity	1.2 Ah
	Energy	3.54 Wh
	Energy Energy	410 Wh kg^{-1}

Table S5. Typical ionic conductivity of SEI components at room temperature.

SEI component	Ionic conductivity at room temperature (S cm^{-1})	Ref.
LMC	$\sim 10^{-9}$	17
LEMC	6.4×10^{-6}	18
Li_2CO_3	10^{-11} to 10^{-8}	19
Li_2O	$\sim 10^{-9}$	20
LiF	ionically insulating	21
Li_3P	$\sim 10^{-4}$	22

As shown in Supplementary Table S5, the values of typical ionic conductivity of conventional SEI components, including LMC, LEMC, Li_2CO_3, Li_2O, and LiF, are much lower than that of Li_3P (~10^{-4} S cm^{-1} at ambient temperature). SEI with rich Li$^+$ conductive species could enable fast Li$^+$ diffusion within it.[17-22]

Table S6. Comparison of the fast-charging capability and cycling performance of reported Si-based anodes with SiO$_x$@P.[23-27]

Areal capacity (mAh cm^{-2})	Rate (C)	Charging time (min)	Charging retention (%)	Cycle number	Capacity retention (%)	Cell type	Ref.
2.0	0.5	120	60	400	30	Coin	23
1.8	3	20	71.4	25	30	Pouch	24
	5	12	77.6	30	35		
1.8	2	120	80.2	300	55	Coin	25
1.6	1	90	87.4	200	80	pouch	26
	4	80	70	100	80		
1.1	3	16.7	80.7	100	200	Coin	27
1.89	4	15	86.5	300	83.2	Pouch	This work
	6	10	83.4	100	85.2		

References

1. P. Dauber-Osguthorpe, V. A. Roberts, D. J. Osguthorpe, J. Wolff, M. Genest, and A. T. Hagler, *Proteins: Structure, Function, and Genetics*, 1988, **4**, 31-47.
2. L. Martínez, R. Andrade, E. G. Birgin and J. M. Martínez, *Journal of Computational Chemistry*, 2009, **30**, 2157-2164.
3. S. Plimpton, *journal of computational physics*, 1995, **117**, 1-19.
4. P. C. Christopher I. Bayly, Wendy D. Cornell, and Peter A. Kollman, *J. Phys. Chem. Lett.*, 1993, **97**, 10269-10280.
5. A. D. William Humphrey, and Klaus Schulten, *Journal of Molecular Graphics* 1996, **14**, 33-38.
6. D. S. M. William L. Jorgensen, Julian Tirado-Rives, *J. Am. Chem. Soc.* , 1996, **118**, 11225-11236.
7. J. D. Jose´ N. Canongia Lopes, Agi´lio A. H. Pa´dua, *Journal of the Physic Chemical B* 2004, **104B**, 2038.
8. T. Lu and F. Chen, *Journal of Computational Chemistry*, 2012, **33**, 580-592.
9. N. Kumar and J. M. Seminario, *The Journal of Physical Chemistry C*, 2016, **120**, 16322-16332.
10. K. Momma and F. Izumi, *Journal of Applied Crystallography*, 2011, **44**, 1272-1276.
11. C. Marino, M. El Kazzi, E. J. Berg, M. He and C. Villevieille, *Chemistry of Materials*, 2017, **29**, 7151-7158.
12. X. Chen, G. Ge, W. Wang, B. Zhang, J. Jiang, X. Yang, Y. Li, L. Wang, X. He and Y. Sun, *Science China Chemistry*, 2021, **64**, 1417-1425.
13. J. Wang, Z. Yang, B. Mao, Y. Wang, Y. Jiang and M. Cao, *ACS Energy Letters*, 2022, **7**, 2781-2791.
14. R. Reinhold, U. Stoeck, H. J. Grafe, D. Mikhailova, T. Jaumann, S. Oswald, S. Kaskel and L. Giebeler, *ACS Appl Mater Interfaces*, 2018, **10**, 7096-7106.
15. SutingWeng, X. Zhang, G. Yang, S. Zhang, B. Ma, Q. Liu, Y. Liu, C. Peng, H. Chen, H. Yu, X. Fan, T. Cheng, L. Chen, Y. Li, Z. Wang and X. Wang, *Nature Communications*, 2023, **14**.
16. A. Ramasubramanian, V. Yurkiv, T. Foroozan, M. Ragone, R. Shahbazian-Yassar and F. Mashayek, *The Journal of Physical Chemistry C*, 2019, **123**, 10237-10245.
17. L. Schafzahl, H. Ehmann, M. Kriechbaum, J. Sattelkow, T. Ganner, H. Plank, M. Wilkening and S. A. Freunberger, *Chemistry of Materials*, 2018, **30**, 3338-3345.
18. L. Wang, A. Menakath, F. Han, Y. Wang, P. Y. Zavalij, K. J. Gaskell, O. Borodin, D. Iuga, S. P. Brown, C. Wang, K. Xu and B. W. Eichhorn, *Nature Chemistry*, 2019, **11**, 789-796.
19. S. Shi, Y. Qi, H. Li and L. G. Hector, *The Journal of Physical Chemistry C*, 2013, **117**, 8579-8593.
20. R. Guo and B. M. Gallant, *Chemistry of Materials*, 2020, **32**, 5525-5533.
21. J. Pan, Y.-T. Cheng and Y. Qi, *Physical Review B*, 2015, **91**.
22. *Solid State Ionics*, 1989, **34**, 97-102.
23. X. Han, Z. Zhang, H. Chen, L. Luo, Q. Zhang, J. Chen, S. Chen and Y. Yang, *Journal of Materials Chemistry A*, 2021, **9**, 3628-3636.
24. M. Je, G. Song, S. Lee, H. J. Park, J. Kim and S. Park, *Journal of Materials Chemistry A*, 2023, **11**, 1694-1703.
25. R. Zhang, Z. Xiao, Z. Lin, X. Yan, Z. He, H. Jiang, Z. Yang, X. Jia and F. Wei, *Nano-Micro Letters*, 2023, **16**.
26. S. Yi, Z. Yan, X. Li, Z. Wang, P. Ning, J. Zhang, J. Huang, D. Yang and N. Du, *Chemical Engineering Journal*, 2023, **473**.
27. M. Han, Y. Mu, L. Wei, L. Zeng and T. Zhao, *Carbon Energy*, 2023, DOI: 10.1002/cey2.377.